PHOTONICS Research

Toward mid-infrared nonlinear optics applications of silicon carbide microdisks engineered by lateral under-etching [Invited]

David Allioux,[1,*] Ali Belarouci,[1,2] Darren Hudson,[3] Eric Magi,[3] Milan Sinobad,[1,4] Guillaume Beaudin,[2] Adrien Michon,[5] Neetesh Singh,[3] Regis Orobtchouk,[1] and Christian Grillet[1,6]

[1]Université de Lyon, Institut des Nanotechnologie de Lyon, 69131 Ecully, France
[2]Department of Electrical Engineering, Université de Sherbrooke, Sherbrooke, QC J1K 2R1, Canada
[3]School of Physics, University of Sydney, Sydney, NSW 2006, Australia
[4]RMIT School of Electrical and Computer Engineering, Melbourne, VIC 3000, Australia
[5]Université Côte d'Azur, CNRS, CRHEA, France
[6]e-mail: Christian.grillet@ec-lyon.fr
*Corresponding author: david.allioux@gmail.com

Received 14 November 2017; revised 22 January 2018; accepted 22 January 2018; posted 23 January 2018 (Doc. ID 310043); published 19 April 2018

We report the fabrication and characterization of silicon carbide microdisks on top of silicon pillars suited for applications from near- to mid-infrared. We probe 10 μm diameter disks with different under-etching depths, from 4 μm down to 1.4 μm, fabricated by isotropic plasma etching and extract quality factors up to 8400 at telecom wavelength. Our geometry is suited to present high Q single-mode operation. We experimentally demonstrate high-order whispering-gallery mode suppression while preserving the fundamental gallery mode and investigate some requirements for nonlinear optics applications on this platform, specifically in terms of quality factor and dispersion for Kerr frequency comb generation.

OCIS codes: (230.5750) Resonators; (130.3120) Integrated optics devices; (190.4400) Nonlinear optics, materials.

https://doi.org/10.1364/PRJ.6.000B74

1. INTRODUCTION

Group IV material is becoming an increasingly important class of dielectric material for integrated photonics, especially for nonlinear applications covering the near- to mid-infrared (IR) range spectrum (from 1 to 12 μm) [1–8]. Silicon (Si) in its conventional silicon-on-insulator (SOI) platform, despite its numerous successes [6,7,9], suffers from several drawbacks, including the high nonlinear absorption of Si and the high absorption losses of silica at wavelengths beyond 3.5 μm [10,11]. This severely limits SOI as a suitable platform for nonlinear applications, in particular in the mid-IR range, and brings the need for an alternative group IV–based platform. Silicon carbide (SiC) is a well-known material especially within the field of high-temperature and high-voltage electronics [12]. It also appears as very promising for nonlinear optics [13–18]. SiC has a high refractive index ($n \approx 2.6$ at $\lambda = 1.55$ μm) [19] allowing a good confinement of the light, and its wide transparency window, from the visible range up to 10–11 μm, makes it suitable for applications from near to mid-IR [20]. It also exhibits high n_2 [18,21,22] and possesses a wide bandgap ($E_g \approx 2.4$ eV) [23] that allows the suppression of two photon absorption beyond 1.1 μm for the 3C cubic structure [16]. SiC has long been very hard to grow and fabricate at the microscale, thus preventing all integrated optics applications. The 3C cubic structure, compared to the more widespread hexagonal ones—4H or 6H—offers the possibility to be grown directly on top of Si [24]. This advantage allows better industrial prospects and the possibility to investigate the mid-IR range where a silica substrate is absorbent. The first demonstration of 3C-SiC grown on a Si substrate in 1995 [24] and its improvement in 2002 to remove the planar defects [25] opened the door to SiC on Si photonics. This has led to a vast variety of designs: from photonic crystals [26] to waveguides [15,27] or microresonators [28–32], all the building blocks of integrated nonlinear photonics.

In this work, we report the fabrication and characterization of SiC microdisks on top of Si pillars. We present a simple approach effectively leading to the suppression of higher radial-order modes while preserving high-quality factor whispering-gallery modes (WGMs). This suppression can be, for instance, beneficial to avoiding modal crossing in Kerr frequency comb generation [33]. Our method is easy to implement, as it uses only an accurate control of the Si pillar lateral under-etching.

We show preliminary experimental results in the linear regime around 1.55 μm via an evanescent coupling technique [34]. Using a silica tapered fiber, we can extract Q factors for two different designs of microdisks with, respectively, 1.4 and 4 μm of lateral under-etching. The obtained values and transmission spectra are supported by simulations and theoretical analysis. Finally, the dispersion engineering of the microdisks is investigated to study the potential of this platform for nonlinear optics applications and specifically the requirements in terms of quality factor and dispersion for Kerr frequency comb generation.

2. DESIGN AND FABRICATION

Our microdisks are designed to exhibit high Q WGMs at IR wavelengths. The main constraint of a SiC on Si platform is that, because Si possesses a higher refractive index than SiC (respectively, $n_{Si} \approx 3.4$ and $n_{SiC} \approx 2.6$ around $\lambda = 1.5$ μm), an adapted geometry is necessary to prevent leakage through the pillar into the Si substrate. We chose a microdisk geometry suspended on a Si pillar to naturally confine the WGMs inside the SiC. We thus overcome the difficulty originating from the high-index platform and this, with reasonable fabrication processes. This geometry is also potentially well suited to accommodate WGMs and enhance nonlinear effects [35]. Simultaneously, we aim to engineer the microdisks to suppress potential higher radial-order WGMs while preserving the quality factor of the fundamental mode. Knowing the difficulties in fabricating SiC structures, we want to avoid the complex geometries that are usually used for single WGM resonators [36]. Instead, we engineer our disks by modifying easily accessible structural parameters, such as the diameter of the disks and the lateral under-etching. A larger pillar leads the higher radial-order modes to leak through it due to their larger effective area. The modeling of the WGMs is performed with a home-made full vectorial finite difference (FVFD) mode solver in cylindrical coordinates [37] and a nine-point discretization scheme. This enables us to accurately simulate the discontinuity of the electromagnetic field tangential components at the boundaries of the microdisk.

In this paper, besides parasitic and coupling losses induced by the fiber in contact with the microdisk, we distinguish four different types of losses: radiation originating from the bending of the edge, scattering that is due to roughness, material absorption, and leakage through the pillar [38]. The mode solver is used to calculate the theoretical maximum intrinsic Q factor achievable with SiC microdisks assuming perfect edges (no sidewall roughness) and a perfectly transparent material, i.e., without scattering and absorption losses. To discriminate between leakage through the pillar and radiation losses and evaluate the impact of the leakage on the maximum theoretical Q factor, we perform FVFD calculations as follows: first on a perfect 10 μm diameter microdisk (smooth edges) surrounded by air without the Si pillar. It allows the determination of the radial modes number and the associated radiative losses. The extremely high-quality factors obtained (greater than 10^{15} for the fundamental modes) show that radiation losses are almost negligible. Second, on the same 10 μm microdisk but sitting on a Si micropillar. Figure 1 shows the evolution

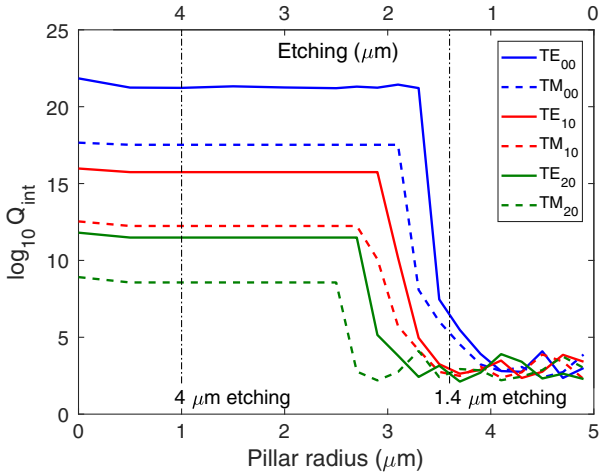

Fig. 1. Evolution of the theoretical intrinsic Q factor with the radius of the pillar at $\lambda = 1.55$ μm for a 10 μm disk with perfect edges. The six radial-order modes with the highest theoretical Q factors and lowest effective areas are plotted. The single-mode operation for the TE mode is achieved with a pillar radius around 3.5 μm.

of losses at $\lambda = 1.55$ μm for a perfect disk without roughness on top of a Si pillar. In this figure, we see that to obtain single-mode operation at $\lambda \approx 1.5$ μm in a 10 μm diameter disk, an under-etching of less than 1.7 μm is necessary. In our case, we decide to focus on two sets of under-etched disks, one with a 4 μm under-etching (pillar radius of 1 μm, therefore highly multimode) and the second with a 1.4 μm under-etching (pillar radius of 3.6 μm). Although a 1.4 μm under-etching affects the Q factor of the fundamental WGMs (see Fig. 1), this value is chosen to ensure the leakage through the pillar i.e., the suppression of higher-order modes typically illustrated in Fig. 2(a).

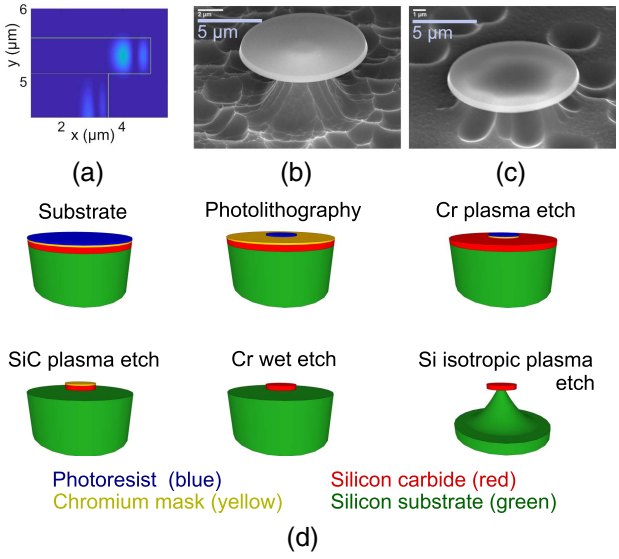

Fig. 2. (a) Intensity mode profile of a simulated WGM at $\lambda = 1.55$ μm in a 10 μm disk with 4 μm lateral under-etching (FVFD mode solver). The mode is a second-order TE mode leaking in the Si. Scanning electron microscope images of 10 μm disks with (b) 4 μm and (c) 1.4 μm lateral under-etching, and (d) fabrication process.

The process flow used for the realization of the microstructures is depicted in Fig. 2(d). SiC microdisk resonators are fabricated using a combination of optical lithography and dry etching processes. The substrate consists of a 500 nm thick 3C-SiC layer epitaxially grown on Si by a standard chemical vapor deposition technique [24,25]. A chromium (Cr) layer with a thickness of 160 nm is evaporated onto the 3C-SiC/Si wafer as a hard mask. The microdisk patterns are then defined in the resist using a standard contact photolithography process. The circular pads are transferred to the Cr mask using inductively coupled plasma (ICP) etching with a chlorine-based plasma, after which the mask is transferred to the SiC layer using ICP etching with a fluorine-based plasma. The Cr mask is subsequently removed using a Cr etchant solution (CR-14). Finally, the edges of the SiC disks are isolated from the Si substrate with an isotropic SF_6-based ICP etch, leaving the resonator suspended by a circular pillar, as shown in Figs. 2(b) and 2(c).

3. EXPERIMENTS

The microdisks are characterized using a well-known evanescent coupling technique [34], sketched in Fig. 3(a). A standard silica fiber is tapered using a butane flame brushing technique down to a 1.2±0.1 μm diameter waist over a 1 cm length. The subwavelength size in this region allows the field to be evanescent, whereas the logarithmic profile of the taper ensures an adiabatic transition that preserves the fundamental fiber mode. Placed in the vicinity of the disk, the light can couple to the WGMs. An amplified spontaneous emission (ASE) light source around 1550 nm connected to the fiber allows us to scan the different WGMs. The polarization of the light is controlled using a polarization controller and an in-line polarizer. As will be described further, due to the large contrast between silica's and SiC's refractive indices, the coupling between the fiber modes and the fundamental WGMs is weak. Also, due to electrostatic effects, when reaching a gap of few micrometers, the fiber is attracted and sticks to the disk. In our configuration, the fiber is in direct contact with the disk. For this reason, determining the coupling strength versus the resonator-fiber gap is not possible. After interacting with the disk, the transmitted light is sent to an optical spectrum analyzer (YOKOGAWA AQ6370 OSA) with a 0.050 nm resolution. As the maximum quality factor recorded never goes beyond 10000, we are not limited by the optical spectrum analyzer resolution. Finally, vertical and horizontal imaging allows us to discriminate the chosen disks and ensures the position control of the fiber, as illustrated in Fig. 3(b).

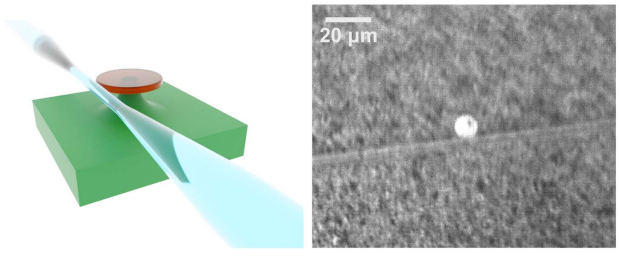

Fig. 3. (a) Scheme of the evanescent coupling technique, and (b) coupling between the tapered fiber and a 10 μm disk.

The first study is done on a disk with 4 μm of Si lateral under-etching, for which the single-mode operation should occur around $\lambda = 4$ μm. This means that the disk is highly multimode around $\lambda \approx 1.55$ μm. To identify the different propagating modes and show their polarization dependence, we modify the polarization from 0° to 170° by increments of 10°. Figure 4(a) shows two of the transmission spectra obtained between 1500 and 1650 nm with a 10 μm diameter disk. This spectrum is obtained by normalizing the power transmitted when the taper touches the microdisk by the power transmitted by the fiber in the air. The dips in the transmission are associated with resonances due to coupling to different radial mode number WGMs inside the microdisk. Using the mode solver, we identify some of the higher-order modes that we wish to suppress. Typically, the dark and green free spectral ranges (FSRs) below the spectrum are associated with the TE_{20} and TE_{40} modes whose power profiles are pictured in Figs. 4(b) and 4(c), respectively.

In Fig. 5(a), we focus specifically on the TM polarization. A linewidth of 0.18 nm is measured for the resonance at $\lambda \approx 1557.9$ nm, leading to a loaded Q factor around $Q_{\text{loaded}} \approx 8400$. This resonance is assumed to be associated to the coupling to the fundamental WGM. The associated

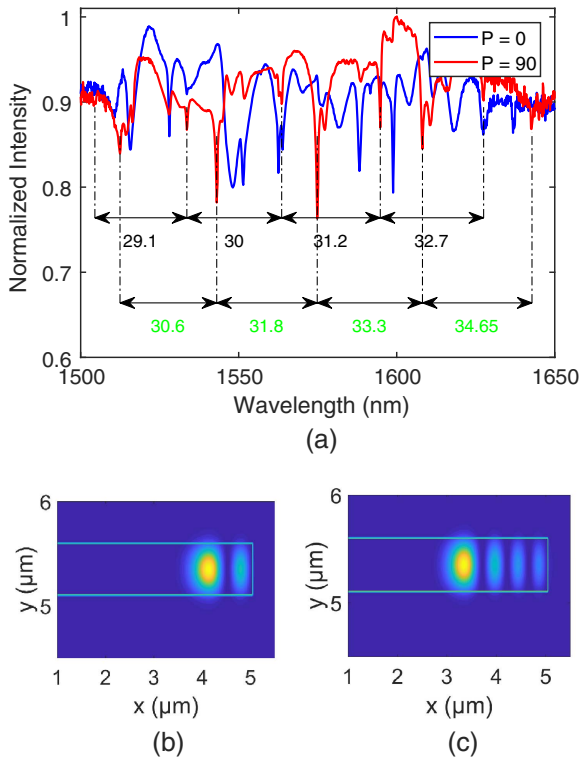

Fig. 4. (a) Experimental transmitted spectrum for a 10 μm diameter disk with 4 μm of lateral under-etching. Two polarizations are plotted: 0° in blue and 90° in red. Note that some modes appear in both polarizations. Below, two FSRs are plotted. Using mode solver, we inferred that they correspond to the TE_{20} modes for the dark one and to the TE_{40} for the green one. The power mode profiles are represented in (b) and (c), respectively.

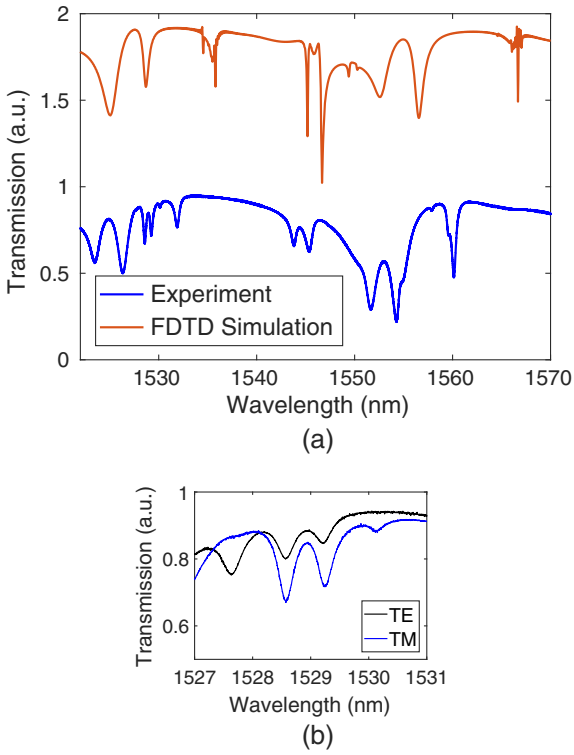

Fig. 5. (a) Experimental (blue) and simulated (red) TM normalized transmitted spectra for a 10 μm diameter disk with 4 μm Si lateral under-etching. (b) TM (blue) and TE (black) polarizations of the transmitted spectra for a 10 μm diameter disk with a 4 μm lateral under-etching.

transmission depth being −0.78 dB, the inferred intrinsic quality factor is very close to the measured one. This very low coupling is mainly due to the strong phase mismatch between the silica taper mode and the fundamental WGM. Using the in-house mode solver simulations (FVFD) presented previously, we can calculate the effective refractive index n_{eff} and the dispersion of the WGMs inside the resonator. A plot of the effective refractive index as a function of the wavelength is shown in Figs. 6(a) and 6(b), respectively, for the 4 μm and for the 1.4 μm Si lateral under-etchings. The dispersion we use is based on the 3C-SiC Sellmeier equation from Ref. [19]. In comparison, the effective index of the 1.2 μm diameter tapered fiber is plotted with a black dashed curve. Comparing

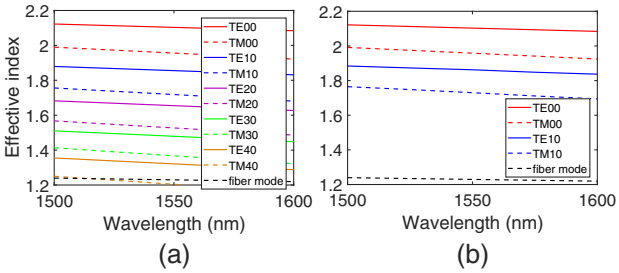

Fig. 6. Effective index as a function of wavelength of the WGMs for a 10 μm disk with (a) 4 μm and (b) 1.4 μm Si lateral under-etching.

the fiber mode effective refractive index ($n_{\text{effFibre}} \approx 1.28$) to the fundamental 10 μm diameter disk WGM ($n_{\text{effWGM}} \approx 2.08$), we can reasonably assume that this particular mode is operating in the under-coupling regime.

We perform 3D finite-difference time-domain (FDTD) simulations with a commercial software (Rsoft Fullwave) that includes the fiber in contact with the microdisk. The obtained spectrum is shown in red in Fig. 5(a). Although some discrepancies between the experiments and simulations are visible, e.g., in terms of the position wavelength and the transmission coefficient, the result's overall aspects are close to one another. In particular, in both the simulation and the experiments, we observe various resonances proving the multimodal behavior of the disks with a 4 μm Si lateral under-etching. We also notice some double-dip shapes. The first interpretation is the well-known splitting of the cavity mode due to the lifting of degeneracy between the clockwise and counterclockwise modes in high Q resonators [39,40] caused by the strong interaction between the disk and the tapered fiber induced by the contact. The other possibility is that the double dips are attributed to the coupling between the TE and TM, as shown in Ref. [41]. Indeed, due to the breaking of symmetry caused by the fiber and the crossing of the two polarization resonance wavelengths, we obtain a strong coupling of the TE and TM modes. This is particularly visible in Fig. 5(b), where we observe three distinct sets of modes. The first corresponds to a TE polarization at $\lambda \approx 1527.7$ nm, the second to a TM polarization at $\lambda \approx 1530.1$ nm, and the third set is a doublet that can be observed for both polarizations at $\lambda \approx 1528.5$ nm and $\lambda \approx 1529.5$ nm.

Using the results of the simulated spectrum, we consider the highest quality factor of the WGMs at $\lambda \approx 1550$ nm and can extract a loaded Q factor around $Q_{\text{loaded}} = 10000$. This value was obtained with a 20 nm roughness corresponding to the simulation discretization step. The experimental quality factors up to 8400 are very close to what we could expect from the simulations, which indicates that the roughness is of the order of a few tens of nanometers. This also shows that there is significant room for improvement in terms of fabrication process that should lead to lower loss, therefore higher Q factor. As already alluded to, we can notice some discrepancies between the experiments and simulations, particularly in terms of the position wavelength and the transmission coefficient. These discrepancies can be attributed to the inexact position and size of the fiber as well as the uncertainty for the SiC refractive index used in our simulation. As the absolute spectral positions of the resonances are proportional to the effective refractive index, these approximations, leading to a small but nonnegligible error in the local effective index and modal distribution, translate into this mismatch between the experimental and simulated results. Typically a few 10^{-3} errors on the refractive index can lead to a shift of ∼5 nm in the spectral resonance position wavelength. However, in terms of the FSR, we can notice that the agreement is relatively good.

We now focus on the microdisk with 1.4 μm Si lateral under-etching. Our objective is to demonstrate that higher-order modes can be suppressed while preserving the fundamental WGM and operating essentially in the single-mode regime.

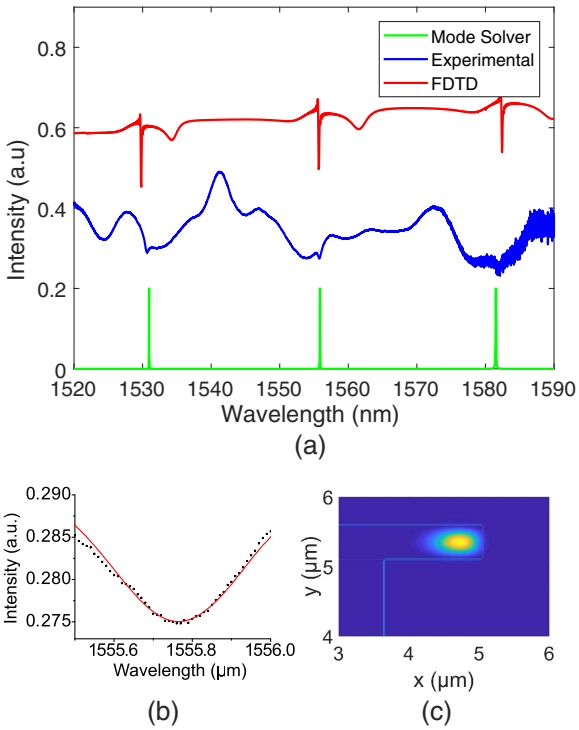

Fig. 7. (a) Experimental transmission spectrum from a 10 μm diameter disk with 1.4 μm Si lateral under-etching in blue. Equivalent simulated transmission spectrum with FDTD in red and mode solver resonances in green. (b) Zoom of the resonance. (c) Power mode profile obtained with mode solver.

The blue curve in Fig. 7(a) shows the transmission spectrum we obtained experimentally. We observe three dips with an FSR of approximately 25.5 nm. We can extract loaded quality factors around $Q_{\text{loaded}} = 4000$ at a resonance wavelength of $\lambda_{\text{res}} = 1555.7$ nm, as shown in Fig. 7(b). As we were expecting for 1.4 μm of lateral under-etching, only one WGM is propagating inside the cavity at a wavelength around $\lambda \approx 1.55$ μm. This result is backed up by the FDTD simulation in red and mode solver in blue in Fig. 7(a). The FSR is very close for both simulations, and the Q factor obtained by FDTD is around $Q_{\text{loaded}} \approx 10200$, corresponding to an intrinsic factor of $Q_{\text{int}} \approx 10700$, confirming the good agreement between simulations and experimental results. We shifted the mode solver and FDTD simulations for better readability by 15 nm. A 15 nm discrepancy is well within the error bar and corresponds to a 1% uncertainty in the refractive index. The good matching shows that we can obtain near-single-mode operation using a simple parameter, which is the lateral under-etching of our microdisks. In our experiments, the Q factor of the fundamental WGM is, as expected (cf. Fig. 1), degraded with a 1.4 μm under-etching compared to a 4 μm. But as indicated previously, Fig. 1 shows that with a good control of the under-etching, the single-mode operation can be achieved with no impact on the quality factor of the fundamental WGM. This study shows that the apparent disadvantage of the lower refractive index of SiC on top of high-index Si substrate can be turned into a new tool for designing integrated components. In a further study, we aim to generalize this approach to mid-IR wavelengths and show the potential of SiC as a candidate for nonlinear IR optics.

4. PERSPECTIVES FOR NONLINEAR OPTICS AND KERR FREQUENCY COMB GENERATION

SiC's good nonlinear properties, i.e., high Kerr coefficient and negligible nonlinear absorption, associated with its high temperature and high power resilience, make it a highly promising nonlinear integrated platform [15,21]. In this section, we theoretically show how, with careful dispersion engineering, our SiC microdisks could potentially be used for nonlinear optics applications and possibly broadband mid-IR frequency comb generation that is useful for a broad range of applications [42].

For broadband frequency comb generation, it is commonly acknowledged that low anomalous group velocity dispersion (GVD, where $D_\lambda = -\frac{\lambda}{C}\frac{d^2n}{d\lambda^2}$, with n the refractive index and C the speed of light) is required [43]. In this section, our objective is to design SiC microdisks capable of operating around a 4 μm pump and close to single-mode operation. A 6 μm under-etching allows us to be close to single-TE-mode operation down to 3 μm wavelength. Toward longer wavelength, the TE mode can propagate up to 6 μm wavelength with low losses. We note that using this geometry, the upper wavelength limit is set by the Si under-etching value rather than the dispersion.

Using the mode solver described in Section 2, we then explore the parameter space (thickness and disk radius) to obtain low anomalous GVD first close to a 4 μm pump wavelength in Fig. 8, and then across a large bandwidth in Fig. 9. Figure 8 shows the evolution of the GVD D_λ as a function of the radius and height of the microdisks at a fixed 4 μm wavelength. The dotted red line indicates the zero of dispersion as well as the 20 and 50 ps/(nm·km) isolines, while the dashed gray lines indicate the effective area of the mode in μm^2. Using this figure, we can find the radius and height to obtain a low anomalous dispersion, typically with $D_\lambda < 20$ ps/(nm·km). We can reach an anomalous dispersion regime for microdisk height between

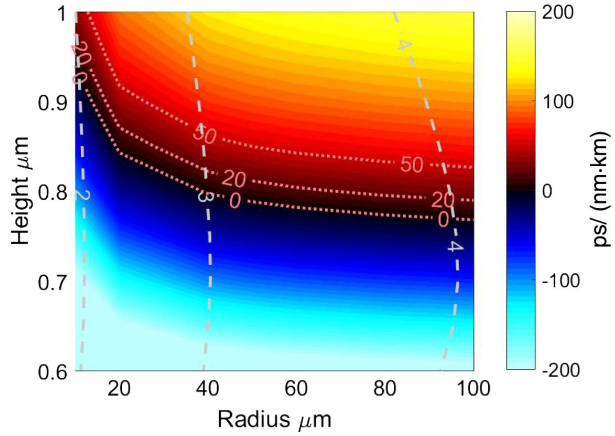

Fig. 8. Group velocity dispersion D_λ evolution with radius (x axis) and height (y axis) for a SiC microdisk at $\lambda = 4$ μm wavelength. The dotted red line indicates the zero of dispersion. The dashed gray lines indicate the effective area of the mode in square micrometers.

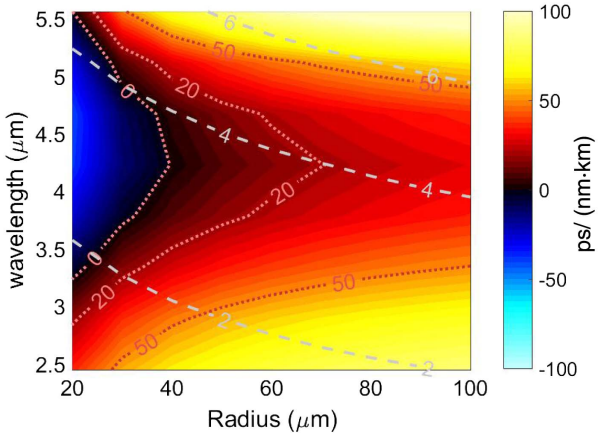

Fig. 9. Dispersion parameter D_λ evolution with radius (x axis) and wavelength (y axis) for a SiC microdisk with a height of 800 nm. The dotted red line indicates the zero of dispersion. The dashed gray lines indicate the effective area of the mode in square micrometers.

800 and 900 nm and radius greater than 40 μm. For instance, an 800 nm thick microdisk leads to a very low dispersion [$D_\lambda < 20$ ps/(nm·km)] for disk radii between 40 and 70 μm. Figure 9 shows the evolution of the GVD for this 800 nm thick disk as a function of the wavelength and disk radii between 20 and 100 μm. Figure 9 emphasizes that an anomalous GVD is possible for a large wavelength span with the right parameter conditions. For instance, we observe that low anomalous dispersion of $D_\lambda < 50$ ps/(nm·km) is achieved from 3.5 to 5.1 μm wavelength for disk radii larger than 40 μm.

Many factors may impact the final device performance. Loss reduction (i.e., enhancing the Q factor) is of course crucial if one wants to generate a broadband comb at a specific repetition rate. To illustrate this, Fig. 10 shows the results obtained from the generalized Lugiato–Lefever Eq. (1) [44] showing the possible generated comb bandwidth and FSR for different Q factors:

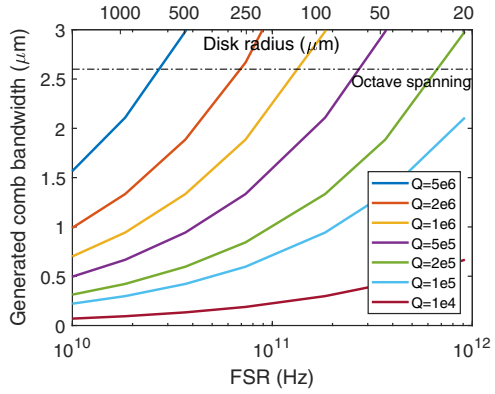

Fig. 10. Theoretical maximum generated frequency comb bandwidth as a function of FSR for a pump power of 1.5 W, a GVD $D_\lambda = 1$ ps/(nm · km), and a wavelength of 4 μm as obtained with Eq. (1). The different curves are for Q factors from 1×10^4 to 5×10^6. The dotted line indicates the bandwidth needed to achieve an octave spanning from 2.7 to 5.4 μm.

$$\Delta f_{\text{theo}} = \frac{0.315}{1.763}\sqrt{\frac{2\gamma P_{\text{in}} Q \lambda_p \text{FSR}}{\pi C|\beta_2|}}. \quad (1)$$

Δf_{theo} stands for the theoretical achievable bandwidth, P_{in} is the pump power that we assumed to be 1.5 W (available, e.g., with MirSense high-power quantum cascade lasers) under critical coupling. λ_p is the pump wavelength assumed to be on-resonance with a mode having a quality factor Q and a free spectral range of FSR. β_2 is the second-order group velocity dispersion, and $\gamma = 2\pi n_2/\lambda_p A_{\text{eff}}$ is the nonlinear parameter, with n_2 the Kerr nonlinear index and A_{eff} the effective area. The coefficient $n_2 \approx 0.5 \times 10^{-18}$ m^2/W is calculated *ab initio* in Refs. [21,22] in the mid-IR and experimentally confirmed in Ref. [18] ($n_2 = 0.531 \times 10^{-18}$ m^2/W) for near-IR wavelengths. Our theoretical predictions show that with quality factors of $Q \approx 10000$, an octave-spanning comb is not achievable. With quality factors of around 2×10^5 (close to what is demonstrated in Ref. [13]), an octave-spanning generated comb can be achieved for a 700 GHz repetition rate. However, we note that for applications requiring few tens of gigahertz spacing, like astronomical spectrograph calibration or optical and microwave waveform synthesis [45], quality factors greater than 10^6 are needed. The best Q factors achieved so far on 3C-SiC are of the order of 5×10^4 [28]. Limitations are mainly due to the roughnesses of the disks but also to the defects of SiC itself [46] formed during the epitaxial process. To achieve Q factors of at least 10^6 that are required for Kerr frequency comb generation, further improvements in epitaxial growth methods and fabrication process are considered to minimize the losses. These optimizations include the use of a pseudo-Si layer to decrease the mismatch at the SiC/Si interface [47], optimizing the gas and temperature [48] during the CVD process, or even switching to amorphous SiC, completely compatible to our needs, that shows a lower n_2 but higher Q factors [49]. In the end, wedge-shaped structures will also be investigated, as they provide a better control of the dispersion as well as a reduction of the scattering losses [50]. This theoretical study shows that this platform is potentially suitable for mid-IR Kerr frequency comb generation but still requires another step of optimization in growth and fabrication processes if we wish to target subhundred gigahertz repetition rate octave spanning.

5. CONCLUSION

We performed a study of SiC microdisks on Si pillars probed by evanescent coupling. We developed an easy and flexible method to suppress high-order modes and obtained high Q single-mode resonators in SiC on Si substrate. We experimentally confirmed a single-mode operation in the near-IR on 10 μm microdisks with a Si lateral under-etching of 1.4 μm. We extracted intrinsic quality factor around 4000 for this fundamental mode. These results were supported by theoretical and simulation studies and showed that our simple approach allowed us to preserve the desired WGM. This approach can be generalized to other low-index materials on high-index substrate platforms, such as diamond on Si. Finally, we theoretically investigated the nonlinear potential of this platform, in particular the requirements for Kerr frequency comb generation in the mid-IR.

Funding. Agence Nationale de la Recherche (ANR) (MIRSICOMB ANR-17-CE24-0028); FP7 People: Marie-Curie Actions (PEOPLE) (PCIGA-2013-631543).

Acknowledgment. This work was supported by the People Program (Marie Curie Actions) of the European Union under REA, the French National Research Agency (project MIRSICOMB ANR-17-CE24-0028), and was conducted within the context of the International Associated Laboratory "ALPhFA: Associated Laboratory for Photonics between France and Australia".

REFERENCES

1. R. Soref, "Mid-infrared photonics in silicon and germanium," Nat. Photonics **4**, 495–497 (2010).
2. L. Carletti, P. Ma, Y. Yu, B. Luther-Davies, D. Hudson, C. Monat, R. Orobtchouk, S. Madden, D. J. Moss, M. Brun, S. Ortiz, P. Labeye, S. Nicoletti, and C. Grillet, "Nonlinear optical response of low loss silicon germanium waveguides in the mid-infrared," Opt. Express **23**, 8261–8271 (2015).
3. L. Carletti, M. Sinobad, P. Ma, Y. Yu, D. Allioux, R. Orobtchouk, M. Brun, S. Ortiz, P. Labeye, J. M. Hartmann, S. Nicoletti, S. Madden, B. Luther-Davies, D. J. Moss, C. Monat, and C. Grillet, "Mid-infrared nonlinear optical response of Si-Ge waveguides with ultra-short optical pulses," Opt. Express **23**, 32202–32214 (2015).
4. N. Singh, D. D. Hudson, Y. Yu, C. Grillet, S. D. Jackson, A. Casas-Bedoya, A. Read, P. Atanackovic, S. G. Duval, S. Palomba, B. Luther-Davies, S. Madden, D. J. Moss, and B. J. Eggleton, "Midinfrared supercontinuum generation from 2 to 6 μm in a silicon nanowire," Optica **2**, 797–802 (2015).
5. C. Grillet, L. Carletti, C. Monat, P. Grosse, B. Ben Bakir, S. Menezo, J. M. Fedeli, and D. J. Moss, "Amorphous silicon nanowires combining high nonlinearity, FOM and optical stability," Opt. Express **20**, 22609–22615 (2012).
6. A. Griffith, R. Lau, J. Cardenas, Y. Okawachi, A. Mohanty, R. Fain, Y. H. D. Lee, M. Yu, C. T. Phare, C. B. Poitras, A. L. Gaeta, and M. Lipson, "Silicon-chip mid-infrared frequency comb generation," Nat. Commun. **6**, 6299 (2015).
7. B. Kuyken, T. Ideguchi, S. Holzner, M. Yan, T. W. Hänsch, J. Van Campenhout, P. Verheyen, S. Coen, F. Leo, R. Baets, G. Roelkens, and N. Picqué, "An octave-spanning mid-infrared frequency comb generated in a silicon nanophotonic wire waveguide," Nat. Commun. **6**, 6310 (2015).
8. C. Y. Wang, T. Herr, P. Del'Haye, A. Schliesser, J. Hofer, R. Holzwarth, T. W. Hänsch, N. Picqué, and T. J. Kippenberg, "Mid-infrared optical frequency combs at 2.5 μm based on crystalline microresonators," Nat. Commun. **4**, 1345 (2013).
9. C. Monat, C. Grillet, M. Collins, A. Clark, J. Schroeder, C. Xiong, J. Li, L. O'Faolain, T. F. Krauss, B. J. Eggleton, and D. J. Moss, "Integrated optical auto-correlator based on third-harmonic generation in a silicon photonic crystal waveguide," Nat. Commun. **5**, 3246 (2014).
10. X. Gai, Y. Yu, B. Kuyken, P. Ma, S. J. Madden, J. Van Campenhout, P. Verheyen, G. Roelkens, R. Baets, and B. Luther-Davies, "Nonlinear absorption and refraction in crystalline silicon in the mid-infrared," Laser Photon. Rev. **7**, 1054–1064 (2013).
11. R. Kitamura, L. Pilon, and M. Jonasz, "Optical constants of silica glass from extreme ultraviolet to far infrared at near room temperature," Appl. Opt. **46**, 8118–8133 (2007).
12. J. B. Casady and R. W. Johnson, "Status of silicon carbide (SiC) as a wide-bandgap semiconductor for high-temperature applications: a review," Solid-State Electron. **39**, 1409–1422 (1996).
13. X. Lu, J. Y. Lee, S. Rogers, and Q. Lin, "Optical Kerr nonlinearity in a high-Q silicon carbide microresonator," Opt. Express **22**, 30826–30832 (2014).
14. H. Sato, M. Abe, I. Shoji, J. Suda, and T. Kondo, "Accurate measurements of second-order nonlinear optical coefficients of 6H and 4H silicon carbide," J. Opt. Soc. Am. B **26**, 1892–1896 (2009).
15. J. Cardenas, M. Yu, Y. Okawachi, C. B. Poitras, R. K. W. Lau, A. Dutt, A. L. Gaeta, and M. Lipson, "Optical nonlinearities in high-confinement silicon carbide waveguides," Opt. Lett. **40**, 4138–4141 (2015).
16. S. Yamada, B. S. Song, J. Upham, T. Asano, Y. Tanaka, and S. Noda, "Suppression of multiple photon absorption in a SiC photonic crystal nanocavity operating at 1.55 μm," Opt. Express **20**, 14789–14796 (2012).
17. S. Wang, M. Zhan, G. Wang, H. Xuan, W. Zhang, C. Liu, C. Xu, Y. Liu, Z. Wei, and X. Chen, "4H-SiC: a new nonlinear material for midinfrared lasers," Laser Photon. Rev. **7**, 831–838 (2013).
18. F. Martini and A. Politi, "Four wave mixing in 3C SiC ring resonators," arXiv:1707.03645 (2017).
19. W. J. Tropf and M. E. Thomas, "Infrared refractive index and thermo-optic coefficient measurement at APL," Johns Hopkins APL Tech. Dig. **19**, 293–297 (1998).
20. H. Mutschke, A. Andersen, D. Clement, T. Henning, and G. Peiter, "Infrared properties of SiC particles," Astron. Astrophys. **345**, 187–202 (1999).
21. F. De Leonardis, B. Troia, R. A. Soref, and V. M. N. Passaro, "Dispersion of nonresonant third-order nonlinearities in silicon carbide," Sci. Rep. **6**, 32622 (2016).
22. D. J. Moss, E. Ghahramani, and J. E. Sipe, "Semi-ab initio tight-binding band-structure calculations of χ^3 (−3ω; ω, ω, ω) in C, Si, Ge, Sic, BP, Alp, AlAs, AlSb, Gap, GaAs, GaSb, InP, InAs, and InSb," Phys. Status Solidi C, **164**, 587–604 (1991).
23. G. L. Harris, *Properties of Silicon Carbide* (INSPEC, the Institution of Electrical Engineers, 1995).
24. C. A. Zorman, A. J. Fleischman, A. S. Dewa, M. Mehregany, C. Jacob, S. Nishino, and P. Pirouz, "Epitaxial growth of 3C-SiC films on 4 in. diam (100) silicon wafers by atmospheric pressure chemical vapor deposition," J. Appl. Phys. **78**, 5136–5138 (1995).
25. H. Nagasawa, K. Yagi, and T. Kawahara, "3C-SiC hetero-epitaxial growth on undulant Si (0 0 1) substrate," J. Crys. Grow. **237–239**, 1244–1249 (2002).
26. S. Yamada, B. S. Song, T. Asano, and S. Noda, "Silicon carbide-based photonic crystal nanocavities for ultra-broadband operation from infrared to visible wavelengths," Appl. Phys. Lett. **99**, 201102 (2011).
27. X. Tang, K. Wongchotigul, and M. G. Spencer, "Optical waveguide formed by cubic silicon carbide on sapphire substrates," Appl. Phys. Lett. **58**, 917–918 (1991).
28. X. Lu, J. Y. Lee, P. X. L. Feng, and Q. Lin, "High Q silicon carbide microdisk resonator," Appl. Phys. Lett. **104**, 181103 (2014).
29. M. Radulaski, T. M. Babinec, K. Mu, K. G. Lagoudakis, J. L. Zhang, S. Buckley, Y. A. Kelaita, K. Alassaad, and G. Ferro, "Visible photoluminescence from cubic (3C) silicon carbide microdisks coupled to high quality whispering gallery modes," ACS Photon. **2**, 14–19 (2015).
30. D. Allioux, A. Belarouci, D. Hudson, N. Singh, E. Magi, G. Beaudin, A. Michon, R. Orobtchouk, and C. Grillet, "Silicon carbide microdisk on silicon pillar probed by evanescent coupling," in *Conference on Lasers and Electro-Optics*, OSA Technical Digest (Optical Society of America, 2016), paper SF2P.1.
31. F. Martini and A. Politi, "Linear integrated optics in 3C silicon carbide," Opt. Express **25**, 10735–10742 (2017).
32. J. Cardenas, M. Zhang, C. T. Phare, S. Y. Shah, C. B. Poitras, B. Guha, and M. Lipson, "High Q SiC microresonators," Opt. Express **21**, 16882–16887 (2013).
33. T. Herr, V. Brasch, J. D. Jost, I. Mirgorodskiy, G. Lihachev, M. L. Gorodetsky, and T. J. Kippenberg, "Mode spectrum and temporal soliton formation in optical microresonators," Phys. Rev. Lett. **113**, 123901 (2014).
34. C. Grillet, E. Magi, and B. J. Eggleton, "Fiber taper coupling to chalcogenide microsphere modes," Appl. Phys. Lett. **92**, 171109 (2008).
35. T. Johnson, "Silicon microdisk resonators for nonlinear optics and dynamics," Ph.D. dissertation (California Institute of Technology, 2009).
36. A. Kordts, M. Pfeiffer, H. Guo, V. Brasch, and T. J. Kippenberg, "Higher order mode suppression in high-Q anomalous dispersion

SiN microresonators for temporal dissipative Kerr soliton formation," Opt. Lett. **41**, 452–455 (2016).
37. M. Masi, R. Orobtchouk, G. Fan, J. M. Fedeli, and L. Pavesi, "Towards a realistic modelling of ultra-compact racetrack resonators," J. Lightwave Technol. **28**, 3233–3242 (2010).
38. V. B. Braginsky, M. L. Gorodetsky, and V. S. Ilchenko, "Quality-factor and nonlinear properties of optical whispering-gallery modes," Phys. Lett. A **137**, 393–397 (1989).
39. T. J. Kippenberg, S. M. Spillane, and K. J. Vahala, "Modal coupling in traveling-wave resonators," Opt. Lett. **27**, 1669–1671 (2002).
40. B. E. Little and J. P. Laine, "Surface-roughness-induced contradirectional coupling in ring and disk resonators," Opt. Lett. **22**, 4–6 (1997).
41. S. Ramelow, A. Farsi, S. Clemmen, J. S. Levy, A. R. Johnson, Y. Okawachi, M. R. E. Lamont, M. Lipson, and A. L. Gaeta, "Strong polarization mode coupling in microresonators," Opt. Lett. **39**, 5134–5137 (2014).
42. A. Schliesser, N. Picqué, and T. W. Hänsch, "Mid-infrared frequency combs," Nat. Photonics **6**, 440–449 (2012).
43. T. J. Kippenberg, R. Holzwarth, and S. A. Diddams, "Microresonator-based optical frequency combs," Science **332**, 555–559 (2011).
44. S. Coen and M. Erkintalo, "Universal scaling laws of Kerr frequency combs," Opt. Lett. **38**, 1790–1792 (2013).
45. S. A. Diddams, "The evolving optical frequency comb," J. Opt. Soc. Am. B **27**, B51–B62 (2010).
46. X. Song, J. F. Michaud, F. Cayrel, M. Zielinski, M. Portail, T. Chassagne, E. Collard, and D. Alquier, "Evidence of electrical activity of extended defects in 3C-SiC grown on Si," Appl. Phys. Lett. **96**, 142104 (2010).
47. R. Khazaka, E. Bahette, M. Portail, D. Alquier, and J. F. Michaud, "Toward high-quality 3C-SiC membrane on a 3C-SiC pseudo-substrate," Mater. Lett. **160**, 28–30 (2015).
48. H. S. Jha and P. Agarwal, "Effects of substrate temperature on structural and electrical properties of cubic silicon carbide films deposited by hot wire chemical vapor deposition technique," J. Mater. Sci. Mater. Electron. **26**, 2844–2850 (2015).
49. X. Lu, J. Y. Lee, P. X.-L. Feng, and Q. Lin, "Silicon carbide microdisk resonator," Opt. Lett. **38**, 1304–1306 (2013).
50. H. Lee, T. Chen, J. Li, K. Y. Yang, S. Jeon, O. Painter, and K. J. Vahala, "Chemically etched ultrahigh-Q wedge-resonator on a silicon chip," Nat. Photonics **6**, 369–373 (2012).